THE JOURNAL OF PHYSICAL CHEMISTRY C

Article

Electrochemical Assessment of the Band-Edge Positioning in Shape-Tailored TiO-Nanorods-Based Photoelectrodes for Dye Solar Cells

Rita Agosta, Roberto Giannuzzi, Luisa De Marco, Michele Manca, Maria Belviso, P Davide Cozzoli, and Giuseppe Gigli

J. Phys. Chem. C, **Just Accepted Manuscript** • DOI: 10.1021/jp304607f • Publication Date (Web): 18 Jan 2013

Electrochemical Assessment of the Band-Edge Positioning in Shape-Tailored TiO_2-Nanorod-Based Photoelectrodes for Dye Solar Cells

Rita Agosta [a⊥], *Roberto Giannuzzi* [a⊥], *Luisa De Marco* [a], *Michele Manca* [a]*, *Maria R. Belviso* [b], *P. Davide Cozzoli* [bc] *and Giuseppe Gigli* [abc]

[a] Center for Bio-Molecular Nanotechnology - IIT Fondazione Istituto Italiano di Tecnologia, Via Barsanti – Arnesano (LECCE) - 73010 - ITALY

[b] National Nanotechnology Laboratory (NNL), CNR Istituto Nanoscienze, Distretto Tecnologico Via Arnesano 16, 73100 Lecce, ITALY

[c] Dipartimento di Matematica e Fisica "E. De Giorgi", Universita' del Salento, Via Arnesano, 73100 Lecce, ITALY

CORRESPONDING AUTHOR E-MAIL: michele.manca@iit.it – tel. +39 0832 295738

[⊥] These authors have contributed equally to this work

KEYWORDS: TiO_2 nanocrystals, photoelectrodes, electrochemical analysis, electron transport

ABSTRACT

Three families of linear shaped TiO_2 anatase nanocrystals with variable aspect ratio (4, 8, 16) and two sets of branched TiO_2 anatase nanocrystals (in the form of open-framework sheaf-like nanorods and compact braid-like nanorod bundles, respectively) were employed to fabricate high-quality mesoporous photoelectrodes and then implemented into dye-sensitized solar cells to elucidate the intrinsic correlation holding between the photovoltaic performances and the structure of the nanocrystal building blocks. To this aim, the chemical capacitance and the

charge-transfer resistance of the photoelectrodes were extrapolated from electrochemical impedance spectroscopy measurements and used to draw a quantitative energy diagram of the dye-sensitized solar cells realized, on the basis of which their photovoltaic performances have been discussed. It has thus been revealed that photoanodes made from braid-like branched-nanorod bundles exhibited the most favorable conditions to minimize recombination at the interface with the electrolyte due to their deep distribution of trap states, whereas linear-shaped nanorods with higher aspect-ratios result in more remarkable downshift of the conduction band edge.

1. INTRODUCTION

Dye-sensitized solar cells (DSSCs) have been the subject of intense study for their high energy conversion efficiency and their interesting working mechanism that differs from that of conventional solar cells, more closely resembling natural photosynthesis.[1]

After more than twenty years of research, DSSC technology has reached enough maturity for viable outdoor applications, as witnessed by the recent achievements on single-junction lab cells exceeding 12% power conversion efficiency (PCE)[2] and long-term stability,[3] as well as on the production of W-connected submodules showing a PCE as high as 8% on active areas as large as 25 cm^2.[4] The low environmental impact, modest cost, reasonably short energy pay-back time, low sensitivity to temperature changes or to the incidence angle of light, performance maintained at low irradiance, and easy implementation onto flexible substrates are some promising features offered by DSSCs over the other device alternatives. Nevertheless, a substantial amount of research work is still needed to fill the gap between today's benchmark conversion efficiency and the Shockley-Queiser (SQ) limit of 32% predicted for a single junction cell.[5] There are in

fact several issues to be highlighted in this regard. For instance, in order to achieve an effective electron-hole separation a supplementary energetic cost has to be paid to facilitate both the electron injection into the conduction band of the oxide semiconductor and the regeneration of the oxidized dye by redox couple. Then, several possible radiative and non-radiative recombination pathways can considerably limit the collection of photogenerated charges. These energetic costs transcribe into a non negligible reduction of the operative open-circuit voltage with respect to the theoretical value estimated by the SQ theory.

The photoelectrode is the key component of a DSSC, since the majority of the photoinduced steps take place in the bulk phase of the underlying semiconductor network or on its surface. Nanoparticle films have been regarded as a paradigm of porous photoelectrodes for use in DSSCs. Nevertheless, nanoparticle films are not thought to offer an ideal structure suitable to electron transport. A major source of non-ideality stands within the fact that electron transport undergoes trapping and detrapping phenomena, i.e., the injected electrons can be captured by trap states and, however, be again thermally emitted back to the conduction band.[6,7] Hence it can be conveniently described with a trap-limited diffusion model. A density of trap states that increases exponentially towards the conduction band edge is found in these nanoporous electrodes.

On the other hand, the lack of a macroscopic electrostatic potential gradient, due to nanoparticle films being permeated with a concentrated electrolyte, ensures that the gradient in electron concentration acts as the main driving force for transport in the mesoporous TiO_2 film, that is, the electron transport occurs by diffusion. Therefore, the charge separation becomes controlled by irreversible chemical charge transfer kinetics.

Recognition of the mechanisms highlighted above has promoted intensive research toward realization of photoanodes made of one dimensional nanocrystalline domains, where an overall reduced number of inter-grain defective interfaces can indeed lead to enhanced transport properties.[8,9,10,11] On the other hand, at relatively large volumes, one dimensional (1D) nanostructures may be less advantageous in terms of dye adsorption capability, relative to their spherical counterparts.[12,13,14] Such drawback can be expected to be, at least partially, offset by exploitation of nanoarchitectures with branched morphologies, in which the anisotropic arm sections are already interconnected prior to the sintering step, thereby allowing minimization of the overall occurrence of defective boundaries with trap states in the photoelectrode. The realization of mesoporous photoanodes built of individual anisotropic nanocrystalline domains with one-dimensional and/or three-dimensional branch-type shapes, where extended electron percolation pathways are available along preferred crystallographic directions and the overall number of inter-grain defective interfaces acting as detrimental carrier traps is reduced, is in fact considered to be an indispensable step toward boosting the performance of DSSCs far beyond the current level.

As of today, only few examples of DSSCs based on colloidal anisotropic nanocrystals with linear nanorod morphology[8,9,10] and mixed linear-branched topologies[15,16,17,20] have been reported, which have shown appreciable light-to-electricity conversion efficiency. With a few exceptions,[17,18,20] no clear correlation could be established between the device performance and the inherent transport properties[15,16,19] due to the huge alteration of the original size-shape features of the nanocrystals utilized,[9] or to the incomplete information on the actual photoelectrode microstructure.[15,16,19] Thus, there is still plenty of scope on synthesizing shape-tailored TiO_2 nanocrystals and clarifying the photoelectron transfer mechanism.

Recently, we demonstrated a general fabrication strategy[10] to DSSCs for which the two main performance-dictating parameters, namely the light-harvesting capability and charge collection efficiency, can be improved and optimized by suitable photoanode engineering.[17,20] We have been able to develop high-quality photoelectrodes based on different families of anisotropic-shaped anatase TiO_2 nanocrystals with finely tailored shapes synthesized by means of advanced surfactant-assisted routes. Linear anatase nanorods with variable aspect ratios and novel breeds of branched anatase nanocrystals (in the form of open-framework sheaf-like nanorods and compact braid-like nanorod bundles, respectively) were employed to fabricate a wide spectrum of mesoporous TiO_2 film photoelectrodes in which the original anatase crystal structure (which is indeed highly preferable for DSSC applications), dimensions and shape of individual nanocrystals were substantially preserved.[17,20] Importantly, the high quality features of the fabricated photoelectrodes allowed us to study the inherent structure-property correlation underlying the device performance, which has so far been elusive in previous works.

In the present paper we report a meticulous analysis of the most relevant electrochemical parameters of such anisotropic-TiO_2-nanocrystal-based DSSCs and deduce an intrinsic correlation between the fundamental electronic properties of the photoelectrodes (transport, recombination, collection efficiency and energy states distribution) and the genuine structure of the TiO_2 building blocks. We purposely chose to deal with mesostructured films which were characterized by the same projected area and the same thickness. Systematic investigations eventually showed that the morphology/size of the particular type of colloidal nanocrystals utilized in the photoelectrode fabrication does make a significant impact on the energetic distribution of the trap states density in the photoanode and allowed to achieve a quantitative assessment of the conduction band-edge energy positioning.

2. EXPERIMENTAL SECTION

2.1 Preparation of TiO_2 nanocrystals

Different samples of organic-capped anatase TiO_2 nanorods (NRs) with linear and branched shapes were prepared according to established literature procedures.

Linear TiO_2 NRs with average diameter of 4 nm and aspect ratio (AR) of 4 and 8 (samples *AR4*-NRs and *AR8*-NRs, respectively), were obtained by low-temperature trimethylamine *N*-oxide catalyzed hydrolysis of titanium isopropoxide (TTIP) in nonanoic acid[21] and oleic acid,[22] respectively. TiO_2 NRs with average AR of 16 (*AR16*-NRs), were obtained by high-temperature nonhydrolytic condensation of TTIP with oleic acid.[23] Branched TiO_2 nanorods with different degree of longitudinal branching and average projected dimensions of 20 x 100 nm and 30 x 200 nm (referred to as *B*-NRs and *BB*-NRs, respectively) were synthesized by sequential aminolytic and pyrolytic decomposition reaction of titanium oleate complexes in oleic acid/oleyl amine mixture at high temperatures.[20] After the synthesis, the TiO_2 nanocrystals were precipitated upon addition of ethanol or 2-propanol: acetone mixtures, separated by centrifugation, and then washed with acetone to remove the excess surfactant residuals. Then, the resulting products were easily redispersible in an apolar organic solvent, such as toluene or chloroform.

2.2 TiO_2 NRs-based paste preparation

Nanocrystal suspensions (containing 4% wt/wt of TiO_2 as revealed by ICP-AES analysis) were stirred at 60°C for 6 h with ethylcellulose previously dissolved in toluene (10% wt/wt).[17,20] Then, terpineol was added and the resulting mixture was stirred again for 1 h.[17,20] Finally toluene was removed by a rotary evaporator to obtain pastes suitable for doctor-blade deposition. The pastes had the following weight percentage composition: TiO_2: 12%; organic capping residual: 15%; ethylcellulose: 5%; terpineol: 68%.

2.3 Fabrication of DSSCs

The TiO_2 pastes were deposited onto FTO glass (10 ohm per sq., provided by Solaronix S.A.) by doctor blading and dried at 160°C for 15 minutes. This procedure was repeated several times in order to obtain the desired film thickness. The film thickness and the dimensions of the active area (0.28 cm^2) were measured using a profilometer.

The electrodes coated with the TiO_2 pastes were gradually heated under an air flow and sintered at 480°C for 30 min. After cooling to 80°C, the TiO_2 electrodes were immersed into a solution of 0.3 mM (bis(tetrabutylammonium)-cis-di(thiocyanato)-N,N'-bis-(4-carboxylato-4'-carboxylic acid-2,2-bipyridine) ruthenium(II) (N719, provided by Solaronix S.A.) in a mixture of acetonitrile and tertbutyl alcohol (v/v, 1 : 1) and kept at room temperature for 14 h.

The solar cells were assembled by placing a platinum-coated conducting glass (counter electrode) on the N719 dye-sensitized photoelectrode (working electrode). The two electrodes were assembled into a sandwich type cell and sealed with a 50 μm thick Surlyn hot-melt gasket. The redox electrolyte was introduced into the inter-electrode void space through a hole pre-drilled on the back of the counter electrode. The holes were sealed up using the Surlyn hot-melt film and a cover glass. The redox electrolyte used was 0.1 M LiI, 0.05 M I_2, 0.6 M 1,2-dimethyl-3-propylimidazolium iodide, and 0.5 M tert-butylpyridine in dried acetonitrile.

2.4 Characterization techniques

Transmission Electron Microscopy (TEM) images of TiO_2 nanocrystals were recorded with Jeol Jem 1011 microscope operating at an accelerating voltage of 100 kV. Scanning Electron Microscopy (SEM) characterization of the TiO_2 photoelectrodes morphology was performed with a RAITH 150 EBL instrument. Typically, the images were acquired at 5 kV accelerating voltages using short exposure times.

The photovoltaic properties of the DSSCs were characterized by recording the photocurrent-voltage (I-V) curves under illumination of A.M. 1.5 (100 mW/cm^2) using a Keithley unit (model 2400 Source Meter). Three parallel samples for each kind of layered structure were realized and tested in DSSCs in order to check measurement reproducibility (which was within 5%).

Electrochemical impedance spectroscopy (EIS) spectra were recorded using an AUTOLAB PGSTAT302N potentiostat operating in a two-electrode mode. Measurements were carried out both in the dark and under illumination at various forward bias voltages in the 300 kHz to 10 mHz frequency range and applying an AC voltage of 10 mV. Bias potentials ranged from 0.5 V to 0.82 V, depending on the open-circuit photopotential of the cell under illumination at 1 sun. The frequency-dependent impedance was fitted by using the Z-view software.

The charge extraction technique was used to estimate the amount of charges stored in the cell under variable working conditions. In particular, cells were kept at open circuit under a given white light intensity supplied using white LEDs (Luxeon, LXML-PWC2). As soon the LED was switched off, the cell was simultaneously short-circuited and the resulting discharge current was integrated to calculate the total charge density in the photoelectrode. In this way the recombination loss during charge extraction could be reasonably neglected. The intensity from the LEDS was controlled by varying the current from a Keithley Source Meter 2440. Light intensity was quoted in 'sun' equivalents calibrated with a spectrally matched silicon photodiode.

3. RESULTS AND DISCUSSION

Surfactant-capped anatase TiO_2 nanocrystals with tailored shape and size were obtained by wet-chemical routes, as previously reported by us.[17,20]. Linear-shaped nanorods with variable aspect ratio, henceforth referred to as sample 'AR4-NRs', 'AR8-NRs' and 'AR16-NRs', respectively

and branched TiO_2 nanorods, henceforth referred to as sample 'B-NRs' and 'BB-NRs' (see TEM insets in Fig. 1 and Table 1), were safely processed with intact geometric features into high-quality mesoporous photoelectrodes (PEs) suitable for DSSCs,[10] as shown by the relevant SEM images in Figure 1.

We studied a set of DSSCs made from such nanocrystals with the aim of deeply understanding the structure-performance relations in such devices. As previously mentioned, the photovoltaic performances of DSSCs are strictly related to the morphology of the original TiO_2 nanocrystals. Their values - for the case of 6 μm-thick photoelectrodes - are listed in Table 1, while the relevant J-V curves are shown in Figure 2. The following observations can be outlined.

First, the trend in the photocurrent density exhibited by PEs assembled from linear NRs with increasing aspect ratio was just opposite to the trend featuring their dye-adsorbing capabilities. This means that inherent electron transport properties of the films overwhelmed the impact of the film surface area (and hence of the dye-loading capability reported in Table 1) on the ultimate photocurrent that could be generated. In particular, the AR16-NRs based film indeed produced the highest photocurrent density value (9.65 mA cm^{-2}) despite their relatively lower surface area. Second, PEs made from sheaf-like B-NRs exhibited dramatically lower values of the photocurrent density (6.80 mA cm^{-2}) with respect to the AR16-NRs, despite they were featured by comparable specific surface area. Third, PEs constituted of large bundles-like, BB-NRs, presented a surprisingly high photocurrent density (8.10 mA cm^{-2}) when taking into account their reduced amount of adsorbed dye molecules. They also provided the highest V_{OC} value (0.82 V) which can be presumably explained as being due to the reduced number of nanocrystal interconnections, hence, of charge-recombination sites. Taken together, these pieces of evidence demonstrate the effectiveness of our film preparation procedure in producing photoelectrodes

that can satisfactorily exploit the intrinsically beneficial transport properties of anisotropically shaped nanocrystals.

With the aim of enlightening the impact of TiO_2 nanocrystal shape and morphology on the transport and recombination properties of the PE, we investigated the electrochemical behavior of our devices by carrying out an accurate electrochemical impedance spectroscopy (EIS) characterization in dark conditions.

EIS is a powerful technique that has been widely employed to investigate the kinetic of electro- and photoelectro-chemical processes occurring in a wide spectrum of functional systems, including DSSCs, which involve a number of coupled processes.[24,25] In the case of nanostructured TiO_2 electrodes, several simultaneous processes contribute to the overall response to a small ac perturbation: (i) the electron transport in the TiO_2, which is influenced by the free carrier density and electron mobility, the latter being probably dependent on the electron motion trap-limited processes; (ii) the transfer of electrons to redox species in the electrolyte, and (iii) the charging of capacitive elements in the high surface area porous structure, including the Helmholtz capacitance in the TiO_2/electrolyte interface and the capacitances associated with filling of the conduction band and surface states of the TiO_2 in the porous structure.

Impedance spectra were analyzed through a well-known equivalent-circuit model that interprets the nanocrystalline TiO_2 film through the transmission line model.[24] In this work, all the electrochemical parameters have been plotted as a function of the corrected potential. As well known indeed, the measured potential needs to be corrected to account for the losses due to the total series resistance R_s, which provides a potential drop that is not associated with the displacement of the Fermi level. It has been calculated as follows:

$$R_s = R_{FTO} + R_{Pt} + R_D \qquad [1]$$

where R_{FTO} is the sheet resistance of FTO glass collector, R_{Pt} is the charge transfer resistance at the platinized counter electrode and R_D is the diffusion resistance in the electrolyte.[26] It was measured at any applied voltage and used to calculate the corresponding V_{corr}:

$$V_{corr} = V_{appl} - JAR_s \quad [2]$$

where A is projected area of cell and J is the flowing current density.

Due to the relatively slow transport through the TiO_2 electrode, recombination of electrons with I_3^- in the electrolyte cannot be neglected. The recombination process always competes with the collection of electrons. Charge recombination can be described by the charge-transfer resistance, R_{CT}, which can be obtained from impedance results. In the dark R_{CT} shows an exponential dependence on the bias voltage, which can be satisfactorily described by the expression:[24,25]

$$R_{CT} = R_0 exp\left(-\beta \frac{eV_{corr}}{k_B T}\right) \quad [3]$$

where β is the transfer coefficient, which was calculated according to the model proposed by Bisquert et al.[27] A reaction order (β), typically in the range of 0.5-0.7, is used to provide an empirical description of sublinear recombination kinetics[27] which takes into account the fact that electrons may be transferred from occupied levels located in the energy gap.[27,28] A value of β ≈ 0.5 was extrapolated for all the families of photoelectrodes, which indicated that no noticeable differences in the recombination's reaction order were associable with nanocrystals featured by any particular morphology.

The logarithmic trend of R_{CT} as a function of the corrected bias voltage is reported in Figure 3. A huge enhancement of R_{CT} was observed for BB-NRs-based photoelectrodes with respect to cells built with other nanocrystal shapes, and in particular with respect to B-NRs.

The electron diffusion resistance, R_T, shown in Figure 4, decreased exponentially with the corrected voltage. Since the R_T is inversely proportional to the density of electrons at the transport level, it is generally expressed in terms of the Boltzmann distribution:[24]

$$R_T = R_{T_0} exp\left[-\frac{e}{k_B T}\left(V_{corr} + \frac{E_{REDOX} - E_c}{e}\right)\right] \quad [4]$$

where R_{T0} is equal for all cells provided that they have similar geometrical dimensions. As expected, the slope of the semi-logarithmic plot resulted in being the same for all the investigated PEs.[29] A value of about 67 mV per decade was drawn, which is in good agreement with the theoretically predicted value of 58 mV per decade[24] at 293.15 K.

The R_T values associated with the various types of PEs were instead found to be significantly diverging: BB-based PEs were characterized by an overall R_T value that was remarkably lower than those corresponding both the linear NRs-based PEs (AR16, AR4, AR8) and their homologous B-NRs.

At this point, it deserves recalling that the absolute values R_T and R_{CT} are of limited usefulness to the purpose of ranking the performances of different devices. For example, R_T and R_{CT} are both extensive parameters that scale with the overall TiO_2 surface area available and additionally depend on the actual number of grain boundaries and lattice defects in the films. As opposed, the R_{CT}/R_T ratio is a more reliable indicator of the genuine electron-collection efficiency of the devices.[30] The competition between the collection and the recombination of electrons can be thus expressed in terms of the electron diffusion length L_n. The latter is generally regarded as the most useful parameter to unambiguously compare the electron transport prerogatives of the photoelectrodes. Nevertheless, it is worthy to emphasize that a rigorous determination of L_n should be performed under specific working conditions.[31]

Coherently with the aim of the present study, the EIS-derived extensive parameters were used to estimate L_n by adopting the quasi-static approximation model proposed by Bisquert et al:[32,33]

$$L_n = d\left(\frac{R_{CT}}{R_T}\right)^{1/2} \quad [5]$$

where *d* is the film thickness.

The extrapolated values of L_n for every PE are plotted in Figure 5 as a function of the corrected voltage. As already reported in our previous work,[17] BB-NRs-based PEs revealed the highest average electron diffusion length, according to the order: BB-PEs > AR16-PEs > AR8-PEs > AR4-PEs > B-PEs. This sequence suggested a corresponding meaningful hierarchy holding among the values of the photo-generated charge carrier collection efficiency. An electron diffusion length that is much larger than the film thickness should be expected to afford a quantitative collection of photo-generated charge carriers.

The charge collection capability of the DSC depends also depends on the ratio of the charge transport and charge recombination resistances. To experimentally support the hypothesis made above we calculated the charge collection efficiency by using the following: [34,35]

$$\eta_{cc} = \left(1 + \frac{R_T}{R_{CT}}\right)^{-1} \quad [6]$$

The extrapolated values of η_{cc} are reported in Table 2.

Furthermore, a careful comparative analysis of the electron recombination rates of the five types of TiO_2 nanostructured films should be based on adequate assessment of the trap states density distribution for each film as well as of the relative positioning of their conduction band (CB)-edges with respect to the redox potential of the electrolyte. To this aim, chemical capacitance and charge-transfer resistance extrapolated from impedance spectroscopy measurements in light

condition enables one to draw a quantitative energy diagram of our photoelectrochemical devices on the basis of which, their photovoltaic performances can be properly discussed.

Figure 6a reports the extrapolated values of the chemical capacitance, C_{meas}, measured under 1 sun illumination at different corrected voltages. At the lower potentials the capacitance is dominated by the Helmholtz layer C_H and by the adsorbed ionic species C_{ad}, whereas at higher ones the chemical capacitance of TiO_2, C_μ, governs the capacitive response of the cell. [24] The latter also exhibits an exponential trend as a function of V_{corr}, which arises from energetic distribution of the trap states density just below the conduction band-edge. Such a distribution is governed by the parameter α (α=T/T_0 where T_0 is the characteristic temperature of the distribution) according to [24, 36]:

$$C_\mu = C_0 exp\left(\frac{\alpha e}{k_B T} V_{corr}\right) \quad [7]$$

In our case the intimate morphology of the TiO_2 building blocks is determining not only the absolute magnitude of this parameter, but even the slope of the logarithmic plot.

The extrapolation of C_μ values thus provides a quantitative assessment of the chemical capacitance of the localized trap states.[7,37] It depends on the density of electronic states (DOS) in TiO_2, g(E), according to following equation:[38]

$$C_\mu = L(1-p)q\ g(E) \quad [8]$$

where L represents the TiO_2 film thickness, p its porosity and

$$g(E) = \frac{\alpha q N_L}{k_B T} exp\left[\frac{\alpha(E-E_C)}{k_B T}\right] \quad [9]$$

with N_L the total density of bandgap states, q the elementary charge, k_B the Boltzmann constant.

The trend observed in Figure 6a allows us to elucidate the effects of surface traps that introduced intraband gap states, the DOS distribution of which is governed by the value of α. Small values of α indicate a broadening of the DOS distribution. The α values for the five different classes of PEs are reported in Table 2. They suggest a corresponding meaningful hierarchy holding among the DOS distribution of the shape-tailored TiO_2 mesostructures. As expected, B-NRs-based PEs revealed the highest value of α, being indicative of a remarkable increase of the trapping phenomena associated with recombination of photogenerated carriers due to shallow distribution of trap states.

To correctly assess the extent of the conduction band-edge shift from the fitting of the DOS distribution, it is also necessary to determine the total trap density (N_L) in the TiO_2 for the five types of photoelectrodes. To this aim we have here implemented the method developed by O'Regan et al.[39] based on the comparison of the charge densities of the different TiO_2 films, that were plotted as a function of the short-circuit photocurrent. The experimental data, which have been obtained by a properly set-up run of charge extraction measurements,[40,41] are reported in Figure 7.

A film with a larger N_L will have more trapped electrons and thus will show a higher number of charges for a given J_{sc}, therefore differences in N_L can be visualized as vertical displacements of the curve.

Anyway N_L is inherently coupled with the position EC (assumed fixed α). Therefore, there is certain flexibility in the use of parameters to fit the data. We arbitrarily choose to fix the value of N_L to $2*10^{20}$ cm^{-3} for the AR4-PEs and set as reference while allowing EC to vary as a fitting parameter.[26,32,40] Relative changes in N_L among the five different families of PEs were hence

determined from Figure 7 by evaluating the entity of the shift with respect to the AR4-PE. The resulting tooling factors are reported in Table 2.

Once N_L values had been estimated, it was possible to draw the DOS distributions of the five different PEs and eventually achieve a quantitative assessment of their conduction band-edge energy positioning, E_C, as sketched in the energy diagram shown in Figure 8. The Fermi level position is indicated by the arrow that marks the extent of V_{OC}. HOMO (-5.45 eV) and LUMO (-3.85 eV) levels of N719 were taken from previously published papers.[42,43] Standard redox energy of 0.518 V vs. NHE has been calculated from the concentration of I^- and I_3^- by means of Nernst's equation. Remarkable differences in terms of position of CB edge were thus revealed among the five PEs: the AR16-PEs was characterized by the lowest value of E_C-E_{REDOX}. Their CB edge was indeed downshifted by about 150 meV with respect to the B-PEs, which in turn exhibited the highest E_C-E_{REDOX} distance.

It is reasonable to expect that a downward shift of the conduction band edge should be beneficial to the injection of photogenerated electrons from the N719 LUMO level. This expectation is well supported by the calculation of the electron concentration (n) in the TiO_2 at open circuit voltage, which are reported in Table 2. It was calculated according to the following:

$$n = \frac{Q}{qL(1-p)} \qquad [10]$$

where Q is the charge stored in the cell ($C*cm^{-2}$).

On the other side, a more favourable electron injection into the TiO_2 conduction band reduces the energy difference E_C-E_F, which reflects the process of charge recombination. These results are also in well agreement with the trend observed for R_{CT} in Figure 6b.

The BB-PEs thus exhibited the most favourable conditions to minimize recombination at the interface with the electrolyte due to their deep distribution of trap states. This feature relies on

the excellent charge-collection efficiency of BB-PEs and basically explains the relatively high photocurrent density they are capable to generate despite their relatively low dye-loading capability. It can be unambiguously ascribed to the particular bundle-like architecture concerned with their monocrystalline nature, where the individual rod-shaped arms are assembled in such a way as to attain crystallographic matching with each other. In contrast, a remarkable increase of the trapping phenomena was observable in the B-PEs, which is associated with a dramatically shallower distribution of trap states. The latter can be reasonably attributed to the presence of tiny monoclinic-phase Ti_5O_5 domains along the nanocrystal arms, which originated during the synthetic process and were believed to act as foreign secondary heterogeneous nucleation centers, from which secondary arms could depart out leading to the hyperbranched topology of the BB-NRs.[20] Ti_5O_5 domains were actually absent in BB-NRs derived from B-NRs.[20] These findings provide a conclusive explanation for the unexpectedly low values of photocurrent density detected for B-NRs-based DSSCs, despite their relatively high dye-loading capability. It can be univocally correlated to the effects of Ti_5O_5 centers, which introduced significant electron losses at the arm boundaries, thus leading to deep intraband gap states.

It is worthy to observe that AR16-PEs exhibited a remarkably lower charge-transport resistance and a deeper DOS distribution with respect to B-PEs, in spite of the fact that both PEs presented almost the same overall surface area (see dye-loading measurements reported in Table 1). This clearly explains the tremendous gap in terms of photovoltaic performances between these two nanostructured PEs. This gap can be evidently justified from the comparison of R_{CT} as a function of the equivalent conduction band potential (see Figure S2 in the Supporting Info Section).

The kinetics of electron transfer to redox level is usually discussed in terms of the apparent charge recombination lifetime τ_n.[36] Figure 9 compares the trends of the apparent electron lifetime τ_n detected at various bias voltages in the light condition. It was calculated by:

$$\tau_n = R_{CT} C_\mu \qquad [11]$$

DSSCs from linear NRs exhibited an easily interpretable trend, which resulted in being in perfect accordance with the effective diffusion length hierarchy highlighted above (Figure 5) as well as with that the trend detected for the charge collection efficiency (Table 2), whereby higher aspect ratios corresponded to longer electron lifetime as a direct consequence of the large chemical capacitance associated with their high density of trap state. BB-PEs were indeed characterized by the longest apparent electron lifetime, but also showed a considerably higher slope with respect to the other families of PEs. As the applied voltage increases, indeed, this gap is progressively filled until, for V_{corr}> 0.71V, AR16-PEs display the absolute longest apparent electron lifetime.

To adequately clarify the latter finding, differences in the densities of the trap state associated to BB-PEs and AR16-PEs have to be taken in to account. As well known,[7] trap states produce a considerable delay in the measured electron lifetime (τ_n) when compared with the lifetime associated to the conduction band free electrons (τ_0). This concept was been mathematically formalized by Bisquert and Vikhrenko assuming the so-called "quasi-static approximation", as follows:

$$\tau_n = \left(1 + \frac{\partial n_t}{\partial n_C}\right)\tau_0 \qquad [12]$$

The term in the brackets, which is proportional to the time which an electron spends in traps states with respect to the time it spends in the conduction band, corresponds to the delay induced by traps at the Fermi level when τ_n is measured. In particular, for a continuous distribution of traps, as the Fermi level progressively raises, electrons occupy progressively deeper traps and the

consequent variation of electron lifetime became stronger.[44] It is so arguable that AR16-PEs, which involve a noticeably broader number of occupied trap states, suffer from a relatively stronger delay effect in the measurements of the electron lifetime with respect to BB-PEs.

On the other hand, the exceedingly low electron lifetime of the B-NRs-based films can be easily explained as being due to their modest C_μ values. This finding also explains their surprisingly low photocurrent densities (see Table I), which were unexpected when considering their relatively larger overall surface area.

4. CONCLUSIONS

We have systematically analyzed the impact of the morphology of five families of shape-tailored TiO_2 anatase nanocrystals on the photovoltaic behavior of high-quality photoelectrodes thereof used in DSSCs. An adequate assessment of the electron transport properties for each film as well as of their relative conduction band positioning has been provided by means of deep analysis of the most relevant electrochemical parameters both in dark and in light conditions.

In particular, we demonstrated that linear nanorods with higher aspect-ratio showed longer electron lifetime as a direct consequence of their specific lattice directionality. Besides, a drastic reduction of the trapping phenomena associated with recombination of photogenerated carriers was observed in the case of bundle-like nanoarchitecture as an effect of the coherent orientation of the crystallographic structure of the single rod arm subunits. Consistently, remarkable differences in the position of conduction band and Fermi level of the five photoelectrodes have been detected. Taken together, our investigations suggest powerful criteria to realize new optimized photoelectrode architectures, for example, by embodying several stacks of differently shaped nanorods with complementary properties.

AKNOWLEDGMENTS

This work has been partially supported by the European project ESCORT - Efficient Solar Cells based on Organic and hybrid Technology (7th FWP—reference number 261920). M. R. Belviso and P.D. Cozzoli acknowledge financial support by the Italian Ministry of Education, University and Research through the project AEROCOMP (contract MIUR no. DM48391). The authors are grateful to Paola Pareo for the morphological characterization of the films and to Prof. Antonino Aricò for many helpful discussions.

Supporting Information Available: Chemical capacitance and recombination resistance at the equivalent CB position taking cell AR4-PEs as a reference. This information is available free of charge via the Internet at http://pubs.acs.org.

REFERENCES

(1) O'Regan, B.; Grätzel, M. A Low-Cost, High-Efficiency Solar Cell Based on Dye Sensitized Colloidal TiO_2 Films. *Nature* **1991**, 353, 737-740.

(2) Yella, A.; Lee, H.; Tsao, H. N.; Yi, C.; Chandiran, A. K.; Nazeeruddin, M.; Diau, E.; Yeh, C.-Y.; Zakeeruddin, S. M.; Grätzel, M. Porphyrin-Sensitized Solar Cells with Cobalt (II/III)–Based Redox Electrolyte Exceed 12 Percent Efficiency. *Science* **2011**, 334, 629-633.

(3) Kuang, D.; Klein, C.; Ito, S.; Moser, J.-E.; Humphry-Baker, R.;Evans, N.; Duriaux, F.; Grätzel, C.; Zakeeruddin, S. M.; Grätzel, M. High-Efficiency and Stable Mesoscopic Dye-Sensitized Solar Cells Based on a High Molar Extinction Coefficient Ruthenium Sensitizer and Nonvolatile Electrolyte. *Adv. Mater.* **2007**, 19, 1133–1137.

(4) Han, L.; Fukui, A.; Chiba, Y.; Islam, A.; Komiya, R.; Fuke, N.; Koide, N.; Yamanaka, R.; Shimizu, M. Integrated Dye-Sensitized Solar Cell Module with Conversion Efficiency of 8.2%. *Appl. Phys. Lett.* **2009**, 94, 013305(1)-013305(3).

(5) Shockley, W.; Quesseir, H. J. Detailed Balance Limit of Efficiency of p-n Junction Solar Cells. *J. Appl. Phys.* **1961**, 32, 510-519.

(6) van de Lagemaat, J.; Frank, A. J. Effect of the Surface-State Distribution on Electron Transport in Dye-Sensitized TiO_2 Solar Cells: Nonlinear Electron-Transport Kinetics. *J. Phys. Chem. B* **2000**, 104, 4292-4294.

(7) Bisquert, J.; Vikhrenko, V. S. Interpretation of the Time Constants Measured by Kinetic Techniques in Nanostructured Semiconductor Electrodes and Dye-Sensitized Solar Cells. *J. Phys. Chem. B* **2004**, 108, 2313-2322.

(8) Jiu, J.; Isoda, S.; Wang, F.; Adachi, M. Dye-Sensitized Solar Cells Based on a Single-Crystalline TiO_2 Nanorod Film. *J. Phys. Chem. B* **2006**, 110, 2087-2092.

(9) Kang, S. H.; Choi, S. H.; Kang, M. S.; Kim, J. Y.; Kim, H. S.; Hyeon, T.; Sung, Y. E. Nanorod-Based Dye-Sensitized Solar Cells with Improved Charge Collection Efficiency. *Adv. Mater.* **2008**, 20, 54-58.

(10) De Marco, L.; Manca, M.; Giannuzzi, R.; Malara, F.; Melcarne, G.; Ciccarella, G.; Zama, I.; Cingolani, R.; Gigli, G. Novel Preparation Method of TiO_2-Nanorod-Based Photoelectrodes for Dye-Sensitized Solar Cells with Improved Light-Harvesting Efficiency. *J. Phys. Chem. C* **2010**, 114, 4228–4236.

(11) Zheng, Q.; Kang, H.; Yun, J.; Lee, J.; Park, J. H.; Baik, S. Hierarchical Construction of Self-Standing Anodized Titania Nanotube Arrays and Nanoparticles for Efficient and Cost-Effective Front-Illuminated Dye-Sensitized Solar Cells. *ACS Nano* **2011**, 5 , 5088–5093.

(12) Fan, K.; Zhang, W.; Peng, T.; Chen, J.; Yang, F. Application of TiO_2 Fusiform Nanorods for Dye-Sensitized Solar Cells with Significantly Improved Efficiency. *J. Phys. Chem. C* **2011**, 115 , 17213–17219

(13) Lee, S.; Cho, I. S.; Lee, J. H.; Kim, D. H.; Kim, D. W.; Kim, J. Y.; Shin, H.; Lee, J. K.; Jung, H. S.; Park, N. G. et al. Two-Step Sol-Gel Method-Based TiO_2 Nanoparticles with Uniform Morphology and Size for Efficient Photo-Energy Conversion Devices. *Chem. Mater.* **2010,** 22, 1958-1965.

(14) Ghadiri, E.; Taghavinia, N.; Zakeeruddin, S. M.; Grätzel, M.; Moser, J. E. Enhanced Electron Collection Efficiency in Dye-Sensitized Solar Cells Based on Nanostructured TiO_2 Hollow Fibers. *Nano Lett.* **2010**, 10, 1632-1638.

(15) Oh, J. K.; Lee, J. K.; Kim, H. S.; Han, S. B.; Park. K. W. TiO_2 Branched Nanostructure Electrodes Synthesized by Seeding Method for Dye-Sensitized Solar Cells. *Chem. Mater.* **2010**, 22, 1114-1118.

(16) Koo, B.; Park, J.; Kim, Y.; Choi, S. H.; Sung, Y. E.; Hyeon, T. Simultaneous Phase- and Size-Controlled Synthesis of TiO_2 Nanorods via Non-Hydrolytic Sol-Gel Reaction of Syringe Pump Delivered Precursors. *J. Phys. Chem. B* **2006**, 110, 24318-24323.

(17) De Marco, L.; Manca, M.; Buonsanti, R.; Giannuzzi, R.; Malara, F.; Pareo, P.; Martinadonna, L.; Giancaspro, N. M.; Cozzoli, P. D.; Gigli, G. High-quality photoelectrodes based on shape-tailored TiO_2 nanocrystals for dye-sensitized solar cells. *J. Mater. Chem.* **2011**, 21, 13371-13379.

(18) Qu, J.; Gao, X. P.; Li, G. R.; Jiang, Q. W.; Yan, T. Y. Structure Transformation and Photoelectrochemical Properties of TiO_2 Nanomaterials Calcined from Titanate Nanotubes. *J. Phys. Chem. C* **2009**, 113, 3359-3363.

(19) Baek, I. C.; Vithal, M.; Chang, J. A.; Yum, J.; Nazeeruddin, Md.K.; Grätzel, M.; Chung, Y.; Seok, S. Facile Preparation of Large Aspect Ratio Ellipsoidal Anatase TiO_2 Nanoparticles and their Application to Dye-Sensitized Solar Cell. *Electrochem. Commun.* **2009**, 11, 909-912.

(20) Buonsanti, R.; Carlino, E.; Giannini, C.; Altamura, D.; De Marco, L.; Giannuzzi, R.; Manca, M.; Gigli, G.; Cozzoli P. D. Hyperbranched Anatase TiO_2 Nanocrystals: Nonaqueous Synthesis, Growth Mechanism and Exploitation in Dye-Sensitized Solar Cells. *J. Am. Chem. Soc.* **2011**, 133, 19216–19239.

(21) De Caro, L.; Carlino, E.; Caputo, G.; Cozzoli, P. D.; Giannini, C. Electron Diffractive Imaging of Oxygen Atoms in Nanocrystals at Sub-Angstrom Resolution. *Nat. Nanotechnol.* **2010**, 5, 360-365.

(22) Cozzoli, P. D.; Kornowski, A.; Weller, H. Low-Temperature Synthesis of Soluble and Processable Organic-Capped Anatase TiO_2 Nanorods. *J. Am. Chem. Soc.* **2003**, 125, 14539-14548.

(23) Joo, J.; Kwon, S. G.; Yu, T.; Cho, M.; Lee, J.; Yoon, J.; Hyeon, T. Large-Scale Synthesis of TiO2 Nanorods via Nonhydrolytic Sol-Gel Ester Elimination Reaction and Their Application to Photocatalytic Inactivation of *E. coli*. *J. Phys. Chem. B* **2005**, 109, 15297-15302.

(24) Wang, Q.; Ito, S.; Grätzel, M.; Fabregat-Santiago, F.; Mora-Sero, I.; Bisquert, J.; Bessho, T.; Imai, H. Characteristics of High Efficiency Dye-Sensitized Solar Cells. *J. Phys. Chem. B* **2006**, 110, 25210-25221.

(25) Fabregat-Santiago, F.; Bisquert, J.; Palomares, E.; Otero, L.; Kuang, D.; Zakeeruddin, S. M.; Grätzel, M. Correlation between Photovoltaic Performance and Impedance Spectroscopy of Dye-Sensitized Solar Cells Based on Ionic Liquids. *J. Phys. Chem. C* **2007**, 111, 6550-6560.

(26) Raga, S. R.; Barea, E. M.; Fabregat-Santiago, F. Analysis of the Origin of Open Circuit Voltage in Dye Solar Cells. *J. Phys. Chem. Lett.* **2012**, 3, 1629-1634.

(27) Bisquert, J.; Mora-Sero, I. Simulation of Steady-State Characteristics of Dye-Sensitized Solar Cells and the Interpretation of the Diffusion Length. *J. Phys. Chem. Lett.* **2010**, 450-456.

(28) Villanueva-Cab, J.; Wang, H.; Oskam, G.; Peter, L. M. Electron Diffusion and Back Reaction in Dye-Sensitized Solar Cells: The Effect of Nonlinear Recombination Kinetics. *J. Phys. Chem. Lett.* **2010**, 1, 748–751.

(29) Fabregat-Santiago, F.; Bisquert, J.; Garcia-Belmonte, G.; Boschloo, G.; Hagfeldt, A. Influence of Electrolyte in Transport and Recombination in Dye-Sensitized Solar Cells Studied by Impedance Spectroscopy. *Sol. Energy Mat. Sol. Cells* **2005**, 87, 117-131.

(30) Hoshikawa, T.; Yamada, M.; Kikuchi, R.; Eguchi, K. Impedance Analysis of Internal Resistance Affecting the Photoelectrochemical Performance of Dye-Sensitized Solar Cells. *J. Electrochem. Soc.* **2005,** 152, E68-E73.

(31) Barnes, P. R. F.; O'Regan B. C. Electron Recombination Kinetics and the Analysis of Collection Efficiency and Diffusion Length Measurements in Dye Sensitized Solar Cells. *J. Phys. Chem. C* **2010**, 114, 19134–19140.

(32) Fabregat-Santiago, F.; Garcia-Belmonte, G.; Mora-Sero, I.; Bisquert, J. Characterization of Nanostructured Hybrid and Organic Solar Cells by Impedance Spectroscopy. *Phys. Chem. Chem. Phys.* **2011**, 13, 9083-9118.

(33) Bisquert, J.; Fabregat-Santiago, F.; Mora-Serò, I.; Garcia-Belmonte, G.; Gimènez, S. Electron Lifetime in Dye-Sensitized Solar Cells: Theory and Interpretation of Measurements. *J. Phys. Chem. C* **2009**, 113, 17278–17290.

(34) Hagfeldt, A.; Boschloo, G.; Sun, L.; Kloo, L.; Pettersson, H. Dye-Sensitized Solar Cells. *Chem. Rev.* **2010**, 110, 6595-6663.

(35) Yum, J.; Baranoff, E.; Kessler, F.; Moehl, T.; Ahmad, S.; Bessho, T.; Marchioro, A.; Ghadiri, E.; Moser, J.; Yi, C.; et al. A cobalt complex redox shuttle for dye-sensitized solar cells with high open-circuit potentials. *Nat. Commun.* **2012**, 3, 631-638.

(36) Fabregat-Santiago, F.; Randriamahazaka, H.; Zaban, A.; Garcia-Canadas, J.; Garcia-Belmonte, G.; Bisquert, J. Chemical Capacitance of Nanoporous-Nanocrystalline TiO_2 in a Room Temperature Ionic Liquid. *Phys. Chem. Chem. Phys.* **2006**, 8, 1827-1833.

(37) Bisquert, J. Chemical Capacitance of Nanostructured Semiconductors: its Origin and Significance for Nanocomposite Solar Cells. *Phys. Chem. Chem. Phys.* **2003**, 5, 5360-5364.

(38) Barea, E. M.; Ortiz J.; Paya, F. J.; Fernandez-Lazaro, F.; Fabregat-Santiago, F.; Sastre-Santos, A.; Bisquert, J. Energetic Factors Governing Injection, Regeneration and Recombination in Dye Solar Cells with Phthalocyanine Sensitizers. *Energy Environ. Sci.* **2010**, 3, 1985-1994.

(39) O'Regan, B.; Xiaoe, L.; Ghaddar, T. Dye Adsorption, Desorption, and Distribution in Mesoporous TiO_2 Films, and its Effects on Recombination Losses in Dye Sensitized Solar Cells. *Energy Environ. Sci.* **2012**, 5, 7203-7215.

(40) Barnes, P. R. F.; Anderson, A. Y.; Juozapavicius, M.; Liu, L.; Li, X.; Palomares, E.; Fornelib, A.; O'Regan, B. C. Factors Controlling Charge Recombination under Dark and Light Conditions in Dye Sensitised Solar Cells. *Phys. Chem. Chem. Phys.* **2011**, 13, 3547–3558.

(41) Duffy, N. W.; Peter, L. M.; Rajapakse, R. M. G.; Wijayantha, K. G. U. A Novel Charge Extraction Method for the Study of Electron Transport and Interfacial Transfer in Dye Sensitized Nanocrystalline Solar Cells. *Electrochem. Commun.* **2000**, 2, 658−662.

(42) Lenzmann, F.; Krueger, J.; Burnside, S.; Brooks, K.; Grätzel, M.; Gal, D.; Ruhle, S.; Cahen, D. Surface Photovoltage Spectroscopy of Dye-Sensitized Solar Cells with TiO_2, Nb_2O_5, and $SrTiO_3$ Nanocrystalline Photoanodes: Indication for Electron Injection from Higher Excited Dye States. *J. Phys. Chem. B* **2001**, 105, 6347-6352.

(43) Grätzel, M. Recent Advances in Sensitized Mesoscopic Solar Cells. *Acc. Chem. Res.* 2009, 42, 1788-1798.

(44) Rose, A. *Concepts in Photoconductivity and Allied Problems*; Interscience: New York, 1963.

TABLES:

Table 1. Nanorod Sizes, Dye Loading and Photovoltaic Performances of DSSCs

Photoelectrode	Nanorod sizes [nm]	Dye Loading [mol*cm^{-2}]	Porosity [%]	η [%]	FF	V_{OC} [V]	J_{sc} [mA/cm^2]
B-PEs	10-20 × 80-100	1.6*10^{-7}	55 %	3.89	0.73	0.78	6.80
BB-PEs	30-50 × 180-200	1.1*10^{-7}	60 %	4.68	0.71	0.82	8.10
AR16-PEs	3-4 × 45-50	1.7*10^{-7}	30 %	5.24	0.70	0.77	9.65
AR8-PEs	4-5 × 35-40	2.0*10^{-7}	25 %	5.20	0.77	0.81	8.36
AR4-PEs	3-4 × 12-14	2.6*10^{-7}	20 %	4.92	0.72	0.79	8.59

Table 2. Charge Collection Efficiency and Energetics

PE	η_{coll}[%]	n at V_{OC}[cm^{-3}]	α	N_L	E_C-E_F[meV]
B-PEs	45	9.96*10^{17}	0.3646	0.79	337
BB-PEs	96	1.22*10^{18}	0.2549	0.89	220
AR16-PEs	80	2.61*10^{18}	0.2746	1.73	198
AR8-PEs	76	1.55*10^{18}	0.3485	1.05	225
AR4-PEs	74	1.52*10^{18}	0.3345	1	245

η_{coll}, collection efficiency under 1 sun illumination at 0.7V; α, slope of chemical capacitance; n, electron density in the TiO_2 at V_{OC} ; Ec-Ef, estimated position of the conduction band edge relatively to Fermi energy level of electrons in the TiO_2 at open circuit conditions.

FIGURES:

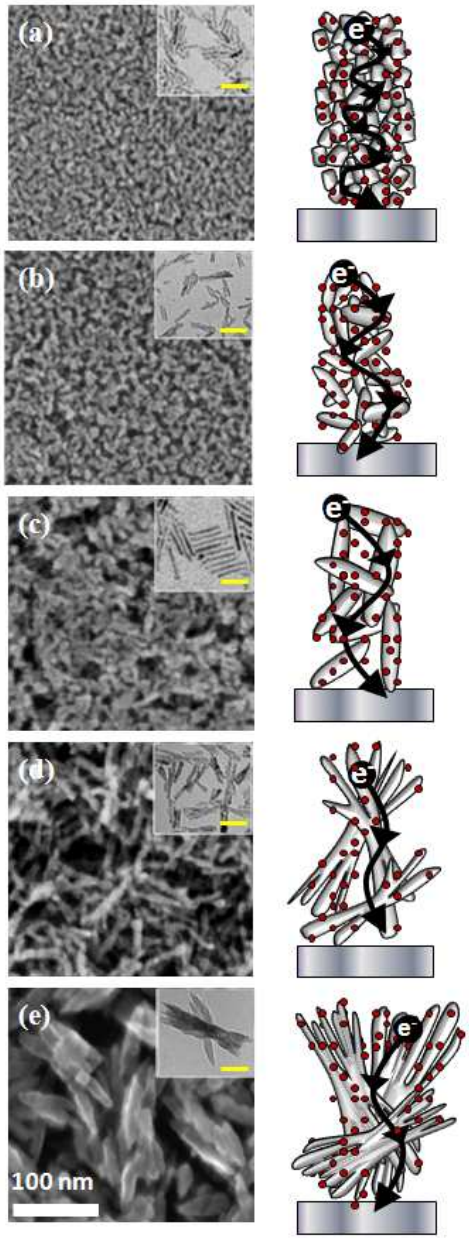

Figure 1 SEM images showing the morphology of the sintered photoelectrodes prepared from AR4-NRs (a), AR8-NRs (b), AR16-NRs (c), B-NRs (d) and BB-NRs (e), along with corresponding sketches highlighting their nano-/microstructure. Inset show TEM images (scale bare 50 nm) of the corresponding nanocrystal employed for the preparation of the photoelectrodes.

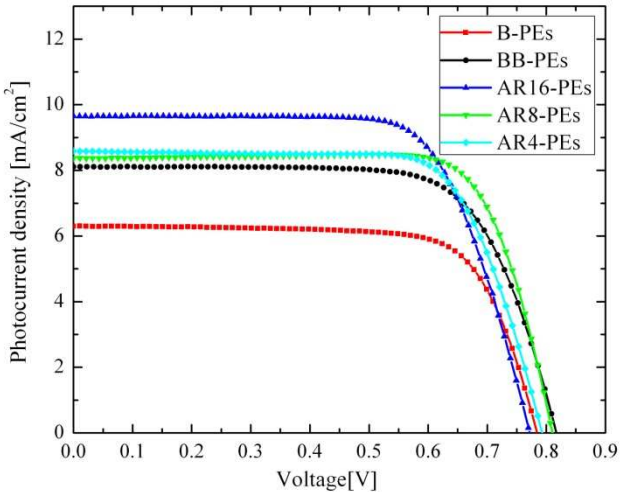

Figure 2 J–V curves of DSSCs implementing 6 μm thick photoelectrodes made of different anisotropic building blocks.

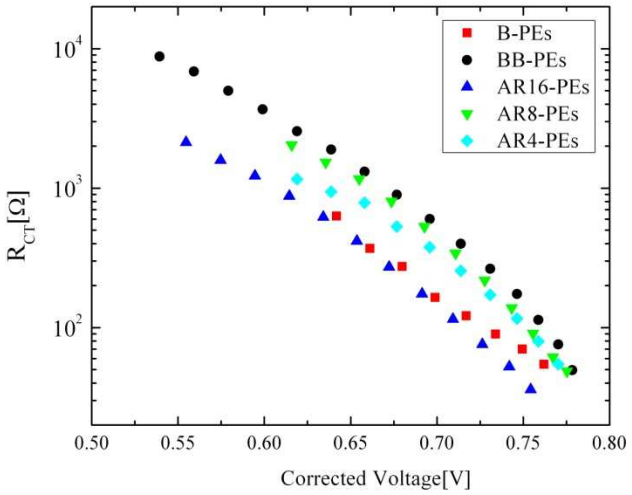

Figure 3 Charge-transfer resistance of the TiO_2 photoelectrode for different devices as a function of the corrected bias voltage obtained from impedance spectra in the dark condition.

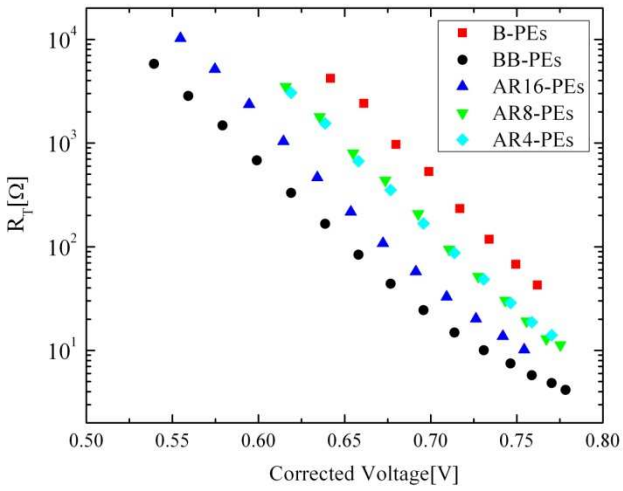

Figure 4 Electron transport resistance of the TiO_2 photoelectrode for different devices as a function of the corrected bias voltage obtained from impedance spectra in the dark condition.

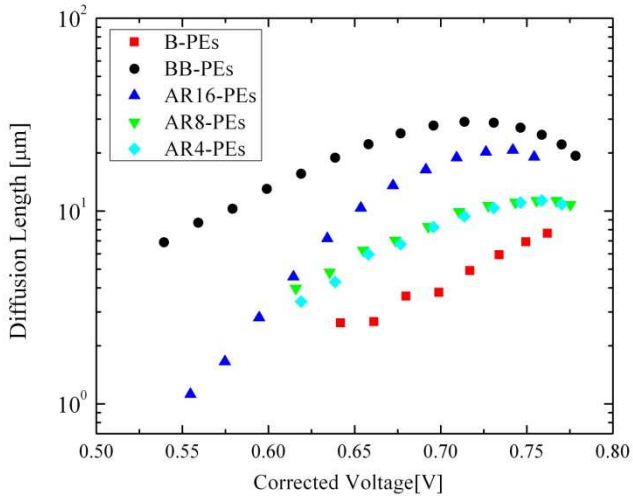

Figure 5 Electron diffusion length in BB-NRs, B-NRs, AR16-NRs, AR8-NRs, AR4-NRs-based photoelectrodes.

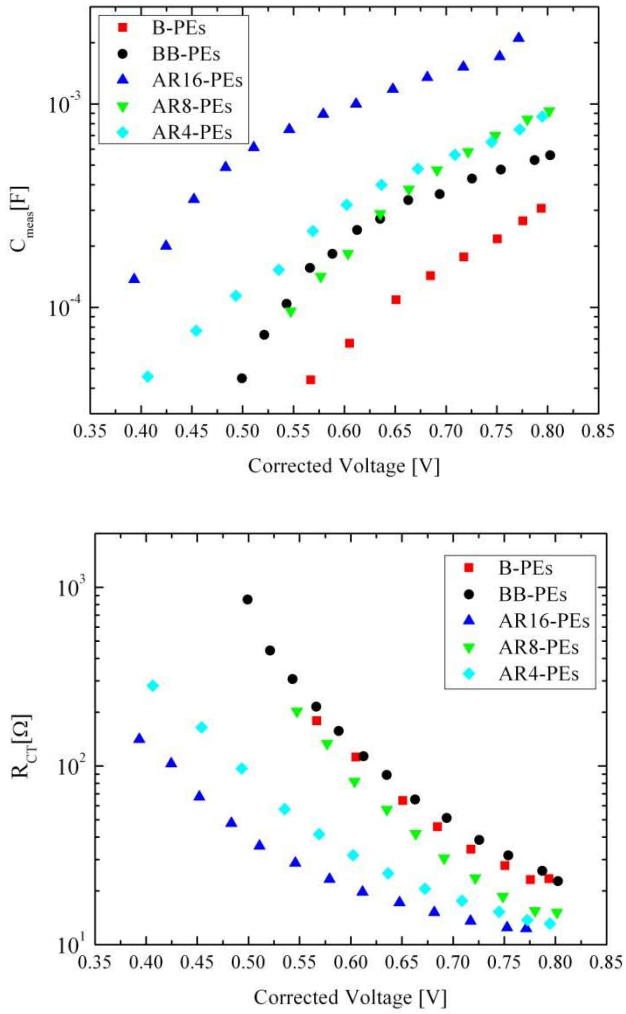

Figure 6 a) Chemical capacitance and b) charge-transfer resistance of the TiO_2 photoelectrode for different devices as a function of the corrected voltage obtained from impedance spectra under 1 sun illumination.

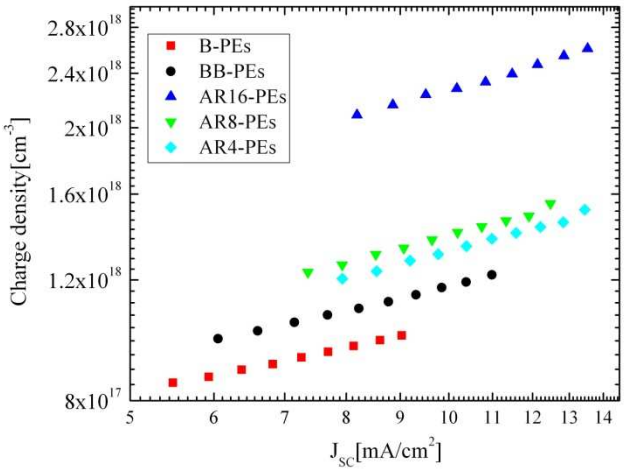

Figure 7 Charge density of the TiO_2 photoelectrodes as a function of short circuit photocurrent.

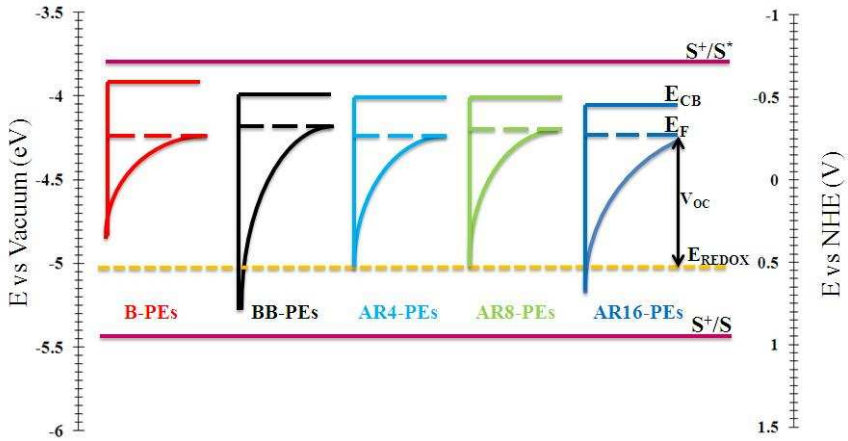

Figure 8 Schematic band energy diagram of position of the TiO_2 conduction band edge energy level (E_{CB}) relative to the Fermi energy level (E_{REDOX}) of the electrolyte and density of electron states below the conduction band of TiO_2 obtained from capacitance measurements.

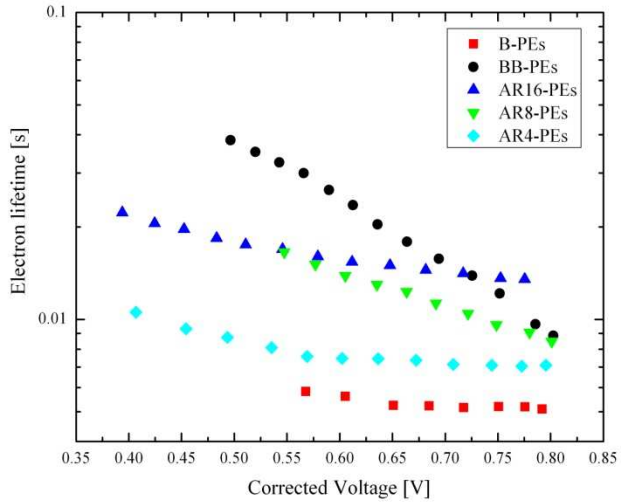

Figure 9 Electron lifetime of the TiO_2 photoelectrode for different devices as a function of the corrected bias voltage obtained from impedance spectra in light.

TABLE OF CONTENTS IMAGE: